Check for updates

JAMES | Journal of Advances in Modeling Earth Systems

RESEARCH ARTICLE
10.1029/2025MS005603

A Subgrid-Scale Parameterization of Wave-Structure Interactions for Spectral Wave Models: Idealized Simulations in Offshore Wind Farm Conditions

Biao Zhao[1,2], Erik Sahlée[1], Jianting Du[3], and Lichuan Wu[1]

[1]Department of Earth Sciences, Uppsala University, Uppsala, Sweden, [2]Program in Atmospheric and Oceanic Sciences, Princeton University, Princeton, NJ, USA, [3]DHI A/S, Hørsholm, Denmark

Key Points:

- A new parameterization is proposed to represent the wave-structure interactions in spectral wave models
- The parameterization represents scattering and drag dominated regimes within a unified framework
- Wave responses exhibit a distinct spatial pattern of upstream amplification and downstream attenuation

Correspondence to:
L. Wu,
lichuan.wu@geo.uu.se

Citation:
Zhao, B., Sahlée, E., Du, J., & Wu, L. (2026). A subgrid-scale parameterization of wave-structure interactions for spectral wave models: Idealized simulations in offshore wind farm conditions. *Journal of Advances in Modeling Earth Systems*, *18*, e2025MS005603. https://doi.org/10.1029/2025MS005603

Received 28 OCT 2025
Accepted 21 JAN 2026

Author Contributions:
Conceptualization: Biao Zhao, Erik Sahlée, Lichuan Wu
Formal analysis: Biao Zhao, Jianting Du
Methodology: Biao Zhao, Jianting Du
Software: Biao Zhao
Supervision: Erik Sahlée, Lichuan Wu
Visualization: Biao Zhao
Writing – original draft: Biao Zhao
Writing – review & editing: Erik Sahlée, Jianting Du, Lichuan Wu

© 2026 The Author(s). Journal of Advances in Modeling Earth Systems published by Wiley Periodicals LLC on behalf of American Geophysical Union. This is an open access article under the terms of the Creative Commons Attribution License, which permits use, distribution and reproduction in any medium, provided the original work is properly cited.

Abstract Extensive offshore renewable energy installations have raised concerns about their environmental impacts. These concerns highlight the need for high fidelity modeling of conditions within wind-farm regions, where wave–structure interactions through reflection, diffraction, and dissipation reshape local and regional wave dynamics, thereby influencing energy conversion efficiency and altering surrounding hydrodynamic conditions. However, accurately representing these wave–structure interactions remains a major challenge for spectral wave models, which often oversimplify turbines as energy sinks and thus introduce nonphysical dissipation. This study develops a new parameterization to represent distinct regimes of wave-structure interactions according to the ratio of wavelength to structural size. When wave and structure scales are comparable, wave scattering dominates and is represented as an energy-conserving source term based on diffraction theory, allowing for directional redistribution of wave energy. Drag-induced dissipation dominates for cases where the wavelength greatly exceeds the structural scale and is parameterized by a dissipative source term. Both regimes are formulated within a unified framework and implemented in the wave spectral model, WAVEWATCH III. Numerical simulations demonstrate that the proposed parameterization improves the physical realism of wave–structure interactions. The modeled wave field exhibits a strong dependence on wave–structure scale ratio and a distinct spatial pattern in significant wave height, with amplification upstream of the farm and attenuation downstream. These findings offer a physics-based solution, supporting future offshore renewable energy development and improving the understanding of its impacts on the marine environment.

Plain Language Summary Offshore wind turbines and wave energy devices interact with ocean waves in complex ways, altering how wave energy is reflected or diffracted. However, most existing spectral wave models oversimplify these cylindrical structures by treating them as energy sinks, removing wave energy without accounting for wave-structure interactions. This can lead to inaccurate representations of the wave field near energy installations. This study presents a new method that better captures these interactions by representing the physical scattering effects of cylindrical structures, such as turbine foundations and wave energy converter devices. The proposed method is based on the classical wave diffraction theory and implemented in WAVEWATCH III, a widely used ocean wave model. It conserves the total wave energy while redistributing it across directions. Simulations using the new scheme reveal a distinct spatial pattern: wave height increases upstream of the wind farm and decreases downstream. This behavior is entirely different from the uniform wave height reduction produced by traditional dissipation-based approaches. This new approach provides a physically based representation of wave-structure interactions for use in wave models and offers a more realistic foundation for modeling wave and wind conditions in offshore renewable energy applications.

1. Introduction

Ocean surface waves play an important role in modulating momentum, heat, and mass exchanges across the air-sea interface (Cavaleri et al., 2012; Janssen, 2004; Wu et al., 2024). With the rapid expansion of offshore renewable energy in recent years, growing attention has been directed toward their potential impacts on the marine environment. Extensive offshore structures, such as wind turbines and wave energy converters, can substantially reshape the local wave field, modifying wave patterns and the distribution of wave energy across the surrounding area. Such modifications have far-reaching implications: they can influence the efficiency of wind energy extraction by altering the boundary layer dynamics (Porchetta et al., 2021), and alter the wave environment essential for energy conversion (Babarit, 2013). Meanwhile, modifications in the wave field induced by these

19422466, 2026, 2, Downloaded from https://agupubs.onlinelibrary.wiley.com/doi/10.1029/2025MS005603 by Uppsala University Library, Wiley Online Library on [04/03/2026]. See the Terms and Conditions (https://onlinelibrary.wiley.com/terms-and-conditions) on Wiley Online Library for rules of use; OA articles are governed by the applicable Creative Commons License

large structural arrays alter the surrounding hydrodynamic environment, resulting in measurable impacts on sediment transport (Neill et al., 2017), benthic habitats, and ecosystem functioning (van Berkel et al., 2020). As offshore renewable projects continue to grow in both scale and spatial extent, understanding their influence on the marine environment has emerged as a key scientific challenge. Nonetheless, wave-structure interactions at the scale of large offshore installations remain poorly represented, even in state-of-the-art spectral models that are well suited for wind-farm or larger scale wave simulations.

Various strategies have been proposed to incorporate sub-grid scale turbine effects into spectral wave models. A common approach is to treat grid cells containing turbines as land points (Alari & Raudsepp, 2012; Ponce de León et al., 2011), thereby imposing a zero-transmission condition that removes the wave energy locally. This simplification ignores the disparity between the turbine size and the model grid scale, leading to an overestimation of energy dissipation when the grid resolution is much coarser than the turbine diameter. To reduce this bias, some studies have refined model resolution to partially resolve the turbine geometry (Hosseini et al., 2025; Zhao et al., 2024). Although this approach can mitigate artificial blocking effects, it still applies uniform attenuation across all wave components, without distinguishing the different responses of waves with varying frequencies and directions to structural interference. Moreover, it remains computationally prohibitive for large-scale applications.

An alternative method introduces a transmission coefficient to parameterize partial energy loss within turbine-containing grid cells (Astariz et al., 2015; David et al., 2022; Venugopal et al., 2017). Compared to land-masking approaches, this allows a portion of the wave energy to propagate through the grid cell, yielding a more moderate downstream decay of wave height. However, a critical limitation of existing approaches lies in their treatment of structures as energy sinks, removing wave energy through nonphysical dissipation and thereby violating wave energy conservation. Similar to the previous land-masking schemes, the transmission-based parameterization fails to resolve the dependence of wave–structure interactions on the ratio of wavelength to structural scale, and consequently cannot account for wave scattering processes such as reflection and diffraction (Porter et al., 2021; Renzi, 2023).

This study aims to address this gap by developing a physically based parameterization to improve the representation of wave-structure interactions in spectral wave models. The proposed parameterization conserves wave energy while capturing directional energy redistribution caused by cylindrical structures-induced wave scattering. A series of idealized simulations is conducted to assess the sensitivity of wave fields to structural and model parameters. The remainder of this paper is organized as follows. Section 2 analyzes wave-structure interaction behavior under different wavelength-to-structure diameter ratios within a framework grounded in diffraction theory. Section 3 presents the formulation of the proposed parameterization and its implementation in the spectral model. Section 4 describes the model setup and experimental design. Section 5 reports the simulation results and key findings. Finally, Section 6 discusses the broader implications of the work and outlines the main conclusions.

2. Theoretical Analysis

When surface gravity waves encounter a fixed offshore structure, part of the wave energy is reflected and part is scattered around the structure, leading to a redistribution of wave energy in the surrounding region. The behavior of this interaction depends mainly on the structure's shape and the relative scale between the structure and the wavelength (Dean & Dalrymple, 1991). When the wavelength is much larger than the structure, the wave field is only slightly disturbed and passes almost unaffected. As the wavelength becomes comparable to the structure scale, strong interference between the incident and scattered waves occurs, causing pronounced diffraction patterns and an intricate spatial distribution of wave amplitude and phase. To analyze these processes from a theoretical perspective, we consider a fixed vertical circular cylinder in an unbounded domain, assuming the flow to be inviscid, incompressible, and irrotational. Under these assumptions, the wave motion can be described within the framework of linear potential flow theory. The wave dispersion relation is given by:

$$\sigma^2 = gk \tanh(kh) \tag{1}$$

where σ represents the wave angular frequency, g is the acceleration of gravity, h is the water depth, and k is the wave number. When a monochromatic plane wave impinges on a vertical cylinder, the wave motion can be described by decomposing the total velocity potential ϕ into two parts (Renzi & Dias, 2012), $\phi = \phi^{\text{scat}} + \phi^{\text{inc}}$,

19422466, 2026, 2, Downloaded from https://agupubs.onlinelibrary.wiley.com/doi/10.1029/2025MS005603 by Uppsala University Library, Wiley Online Library on [04/03/2026]. See the Terms and Conditions (https://onlinelibrary.wiley.com/terms-and-conditions) on Wiley Online Library for rules of use; OA articles are governed by the applicable Creative Commons License

where ϕ^{inc} and ϕ^{scat} denote the incident and scattered potentials. Building on this decomposition, the scattered component is determined using wave diffraction theory (MacCamy & Fuchs, 1954). Accordingly, the velocity potential of the scattered waves in polar coordinates can be expressed as:

$$\phi^{\text{scat}}(\sigma,r,\theta,z) = \frac{gH}{2\sigma}\frac{\cosh(k(h+z))}{\cosh(kh)}\left[\frac{J_0'(ka)}{H_0^{(1)\prime}(ka)}H_0^{(1)}(kr) + \sum_{m=1}^{\infty}2i^m\cos(m(\theta-\theta_0))\left(\frac{J_m'(ka)}{H_m^{(1)\prime}(ka)}H_m^{(1)}(kr)\right)\right]e^{-i\sigma t} \tag{2}$$

where r denotes the radial distance from the center of the cylindrical structure in the horizontal plane, and θ represents the azimuthal angle measured around the structure. z and t represent the vertical coordinate and time, respectively. H is the incident wave height, and a is the radius of the cylinder. The angle θ_0 defines the incident-wave direction with respect to the coordinate system. The symbol $i = \sqrt{-1}$ is the imaginary unit, and $e^{-i\sigma t}$ describes the temporal phase of the wave motion, governing the oscillation of the wave field with angular frequency σ. The integer $m (= 0, 1, 2, \dots)$ denotes the angular mode number. J_m and $H_m^{(1)}$ denote the Bessel and Hankel functions of the first kind of order m, respectively, and the primes indicate differentiation with respect to their arguments. In particular, J_0 and $H_0^{(1)}$ correspond to the first kind of Bessel and Hankel functions at $m = 0$. The ratio $\cosh[k(h+z)]/\cosh(kh)$ represents the vertical structure of the potential, characterizing the exponential decay of the wave-induced motion with depth h. The factor $2i^m\cos[m(\theta-\theta_0)]$ describes the azimuthal variation of each angular mode around the cylinder. For $m = 0$, the term reduces to unity, corresponding to the axisymmetric mode, whereas higher-order modes ($m \geq 1$) represent nonaxisymmetric components of the scattered field. Collectively, these terms express the scattered-wave potential that satisfies the no-normal-flow boundary conditions on the cylindrical surface within the framework of wave diffraction theory.

Using the scattered potential given in Equation 2 and applying the linearized free-surface boundary condition $\eta = -\frac{1}{g}\frac{\partial\phi^{\text{scat}}}{\partial t}|_{z=0}$, the scattered surface elevation is obtained as:

$$\eta^{\text{scat}}(\sigma,r,\theta) = \frac{iH}{2}\left[\frac{J_0'(ka)}{H_0^{(1)}(ka)}H_0^{(1)}(kr) + \sum_{m=1}^{\infty}2i^m\cos(m(\theta-\theta_0))\left(\frac{J_m'(ka)}{H_m^{(1)}(ka)}H_m^{(1)}(kr)\right)\right]e^{-i\sigma t} \tag{3}$$

According to the potential flow theory, the velocity field is given by the gradient of the velocity potential, $\mathbf{u} = \nabla\phi$. Consequently, by taking partial derivatives of ϕ^{scat} with respect to r, θ, and z,

$$u_r^{\text{scat}}(\sigma,r,\theta,z) = \frac{\partial\phi^{\text{scat}}}{\partial r}, u_\theta^{\text{scat}}(\sigma,r,\theta,z) = \frac{1}{r}\frac{\partial\phi^{\text{scat}}}{\partial\theta}, u_z^{\text{scat}}(\sigma,r,\theta,z) = \frac{\partial\phi^{\text{scat}}}{\partial z} \tag{4}$$

the radial, angular, and vertical components of the scattered velocity are derived as follows:

$$u_r^{\text{scat}}(\sigma,r,\theta,z) = \frac{gH}{2\sigma}\frac{\cosh(k(h+z))}{\cosh(kh)}\left[\frac{J_0'(ka)}{H_0^{(1)\prime}(ka)}H_0^{(1)\prime}(kr) + \sum_{m=1}^{\infty}2i^m\cos(m(\theta-\theta_0))\left(\frac{J_m'(ka)}{H_m^{(1)\prime}(ka)}H_m^{(1)\prime}(kr)\right)\right]e^{-i\sigma t} \tag{5}$$

$$u_\theta^{\text{scat}}(\sigma,r,\theta,z) = -\frac{1}{r}\frac{gH}{2\sigma}\frac{\cosh(k(h+z))}{\cosh(kh)} \times\left[\sum_{m=1}^{\infty}2i^m m\sin(m(\theta-\theta_0))\left(\frac{J_m'(ka)}{H_m^{(1)}(ka)}H_m^{(1)}(kr)\right)\right]e^{-i\sigma t} \tag{6}$$

$$u_z^{\text{scat}}(\sigma,r,\theta,z)=\frac{gH}{2\sigma}\frac{k\sinh(k(h+z))}{\cosh(kh)}\left[\frac{J_0'(ka)}{H_0^{(1)'}(ka)}H_0^{(1)}(kr)+\sum_{m=1}^{\infty}2i^m\cos(m(\theta-\theta_0))\left(\frac{J_m'(ka)}{H_m^{(1)}(ka)}H_m^{(1)}(kr)\right)\right]e^{-i\sigma t} \tag{7}$$

The velocity components defined above describe the periodic motion of fluid particles around the structure and therefore determine how the scattered wave energy is distributed in space. Based on these velocities, the total kinetic energy of the scattered wave contained in the water column of radius R surrounding the structure can be evaluated as

$$e_k^{\text{scat}}(\sigma)=\frac{1}{2}\rho\int_{-h}^{0}\int_{0}^{2\pi}\int_{a}^{R}\left[\left(u_r^{\text{scat}}\right)^2+\left(u_\theta^{\text{scat}}\right)^2+\left(u_z^{\text{scat}}\right)^2\right]rdrd\theta dz \tag{8}$$

Similarly, the potential energy of the scattered wave in the same region is given by

$$e_p^{\text{scat}}(\sigma)=\frac{1}{2}\rho g\int_{0}^{2\pi}\int_{a}^{R}\left(\eta^{\text{scat}}\right)^2rdrd\theta. \tag{9}$$

In parallel, the corresponding velocity potential of incident wave field, expressed in cylindrical coordinates (r,θ,z) centered at the structure, is given by

$$\phi^{\text{inc}}(\sigma,r,\theta,z)=\frac{gH}{2\sigma}\frac{\cosh(k(h+z))}{\cosh(kh)}e^{-i\,(kr\,\cos(\theta-\theta_0)-\sigma t)} \tag{10}$$

From this potential, the corresponding free-surface elevation and the velocity components in the radial, azimuthal, and vertical directions are obtained as

$$\eta^{\text{inc}}(\sigma,r,\theta)=\frac{iH}{2}e^{-i\,(kr\,\cos(\theta-\theta_0)-\sigma t)} \tag{11}$$

$$u_r^{\text{inc}}(\sigma,r,\theta,z)=\frac{ikgH}{2\sigma}\frac{\cosh(k(h+z))}{\cosh(kh)}\cos(\theta-\theta_0)\,e^{-i\,(kr\,\cos(\theta-\theta_0)-\sigma t)} \tag{12}$$

$$u_\theta^{\text{inc}}(\sigma,r,\theta,z)=-\frac{ikgH}{2\sigma}\frac{\cosh(k(h+z))}{\cosh(kh)}\sin(\theta-\theta_0)\,e^{-i\,(kr\,\cos(\theta-\theta_0)-\sigma t)} \tag{13}$$

$$u_z^{\text{inc}}(\sigma,r,\theta,z)=\frac{gH}{2\sigma}\frac{k\sinh(k(h+z))}{\cosh(kh)}e^{-i\,(kr\,\cos(\theta-\theta_0)-\sigma t)} \tag{14}$$

Following the same definitions as for the scattered wave, the kinetic and potential energies of the incident wave within the water column of radius R are estimated by:

$$e_k^{\text{inc}}(\sigma)=\frac{1}{2}\rho\int_{-h}^{0}\int_{0}^{2\pi}\int_{a}^{R}\left[\left(u_r^{\text{inc}}\right)^2+\left(u_\theta^{\text{inc}}\right)^2+\left(u_z^{\text{inc}}\right)^2\right]rdrd\theta dz \tag{15}$$

$$e_p^{\text{inc}}(\sigma)=\frac{1}{2}\rho g\int_{0}^{2\pi}\int_{a}^{R}\left[\eta^{\text{inc}}\right]^2rdrd\theta \tag{16}$$

Naturally, based on the expressions of the incident and scattered wave fields given above, the total surface elevation is expressed as

$$\eta^{\text{total}}(\sigma,r,\theta)=\eta^{\text{inc}}(\sigma,r,\theta)+\eta^{\text{scat}}(\sigma,r,\theta) \tag{17}$$

19422466, 2026, 2, Downloaded from https://agupubs.onlinelibrary.wiley.com/doi/10.1029/2025MS005603 by Uppsala University Library, Wiley Online Library on [04/03/2026]. See the Terms and Conditions (https://onlinelibrary.wiley.com/terms-and-conditions) on Wiley Online Library for rules of use; OA articles are governed by the applicable Creative Commons License

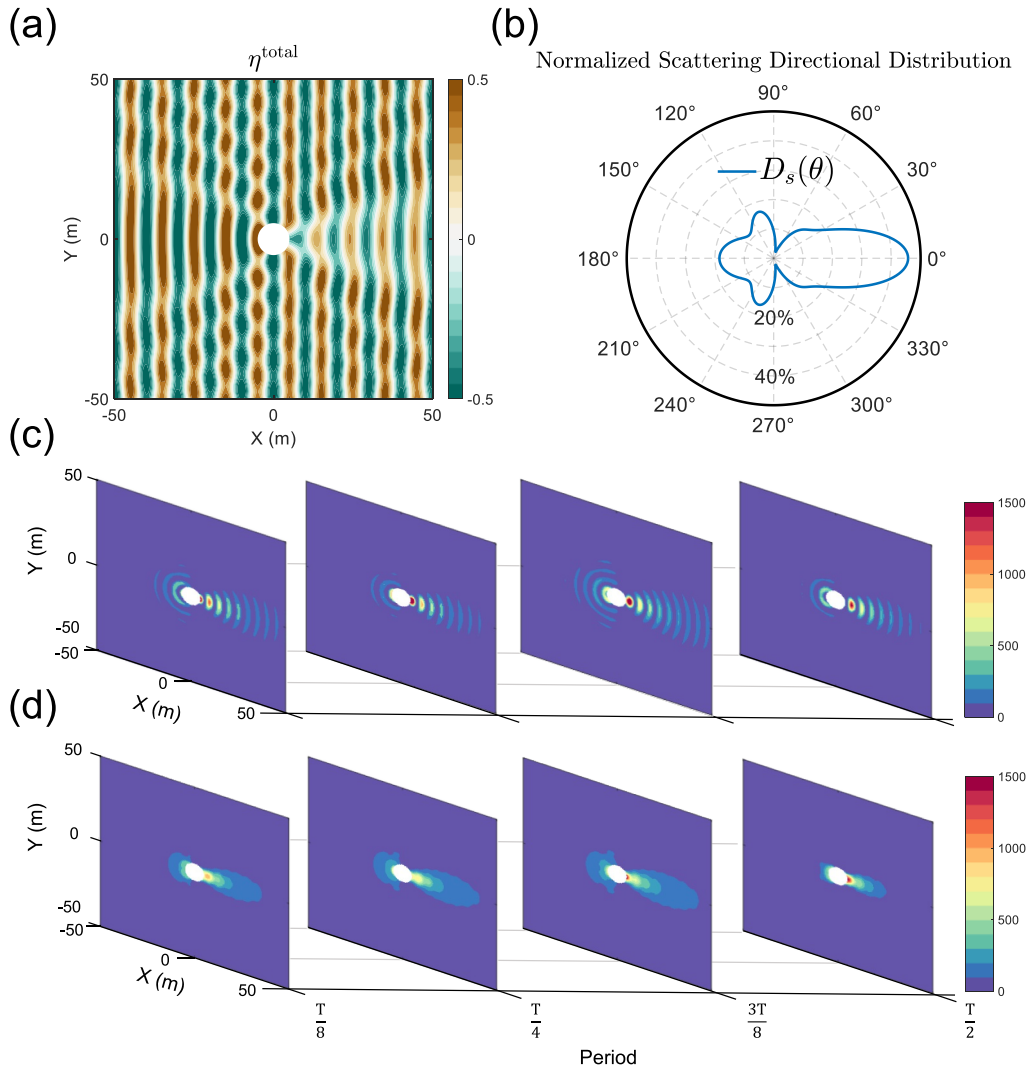

Figure 1. Surface elevation and energy distributions for the case of $\lambda/D = 1$. (a) Total surface elevation (m), (b) normalized scattering directional distribution function, (c) potential energy of scattered wave (J m^{-2}), and (d) kinetic energy of scattered wave (J m^{-2}). The structure is located at the center; the incident wave propagates from left to right.

Building upon the theoretical formulations presented above, we now analyze the scattering characteristics of surface waves interact with a fixed vertical cylinder. The analysis considers a constant water depth of $h = 20$ m, which is representative of typical offshore wind farm sites. The incident wave height H is set to 1 m, and a cylinder diameter to $D = 10$ m (radius $a = 5$ m). To examine the influence of relative wave scale, three wavelength-to-diameter ratios are investigated, $\lambda/D = 1$, 3, and 5, respectively. For each case, the total kinetic and potential energies of the scattered wave field are evaluated by integrating over the entire water column and radially from the cylinder surface ($r = a$) to an outer radius of $R = 250$ m, according to Equations 8 and 9. The selected radius $R = 250$ m represents the local domain around a single turbine within a regular turbine array, corresponding to half of the typical turbine spacing (usually 500 m) in offshore wind farms.

Figure 1a illustrates the total elevation pattern resulting from the superposition of the incident and scattered waves for the case of $\lambda/D = 1$. The incident wave propagates from left to right as a plane wave, and its interaction with the cylindrical structure produces pronounced interference patterns. An enhanced wave amplitude is observed in front of the structure, while a reduction occurs in the lee region due to the redistribution of wave energy away from the structure (Figures 1c and 1d). The kinetic and potential energy fields vary periodically in time with a period of

19422466, 2026, 2, Downloaded from https://agupubs.onlinelibrary.wiley.com/doi/10.1029/2025MS005603 by Uppsala University Library, Wiley Online Library on [04/03/2026]. See the Terms and Conditions (https://onlinelibrary.wiley.com/terms-and-conditions) on Wiley Online Library for rules of use; OA articles are governed by the applicable Creative Commons License

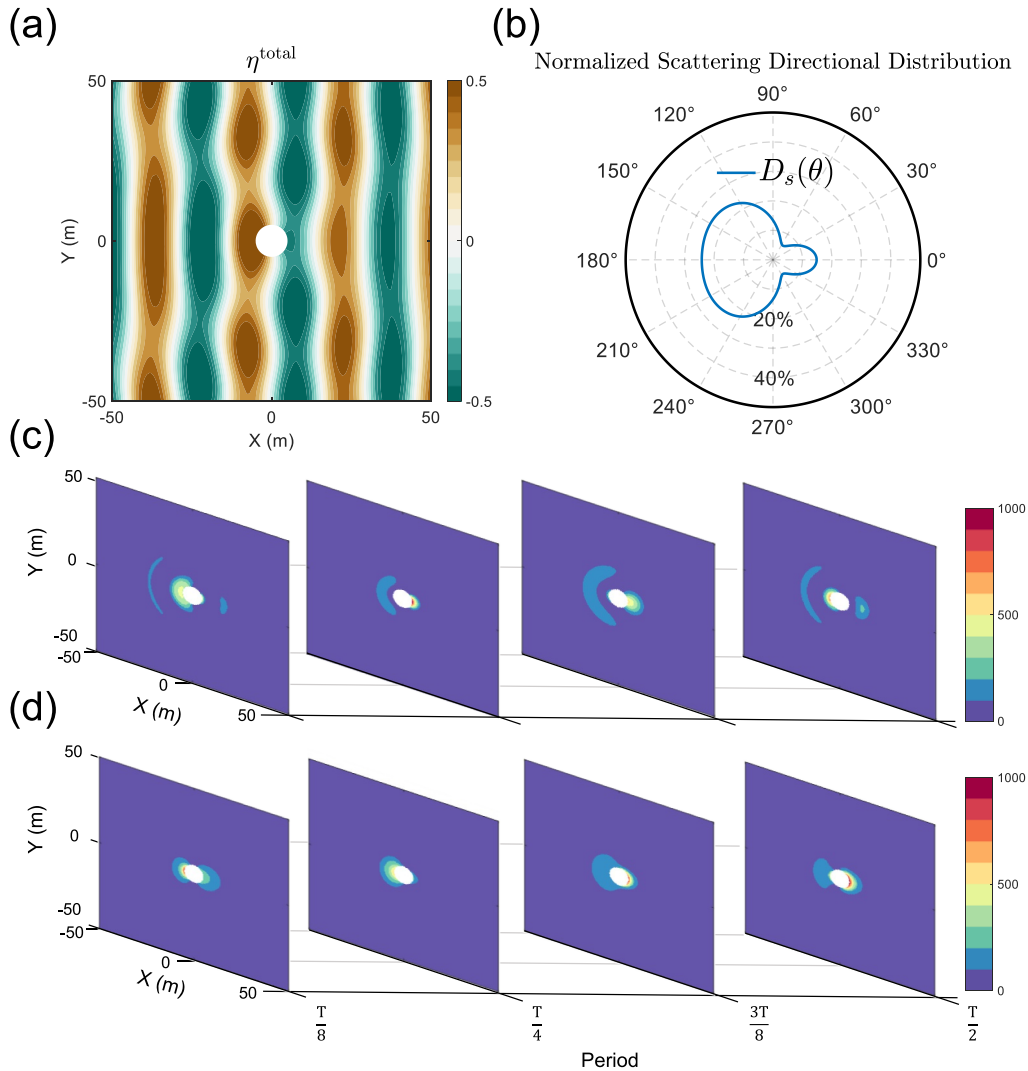

Figure 2. Same as Figure 1, but for $\lambda/D = 3$.

$T/2$, reflecting their quadratic dependence on surface elevation and velocity. This temporal behavior is fully consistent with linear wave theory. The scattered wave energy exhibits a strongly anisotropic spatial distribution, with a dominant forward lobe (0°) aligned with the incident wave direction, characteristic of diffraction around the structure. The backscattered energy near 180° is relatively weak, while secondary lobes appear near the lateral directions (90° and 270°). Overall, the pattern is symmetric with respect to the incident wave axis and reflects the contribution of multiple angular scattering modes.

Figures 2a and 3a show the total surface elevation fields for the cases of $\lambda/D = 3$ and $\lambda/D = 5$, respectively. Compared to the case of $\lambda/D = 1$, the interference pattern around the structure becomes progressively simpler as λ/D increases. For $\lambda/D = 3$, the enhancement of sea surface elevation is still observed on the upstream side, while a weaker interference pattern persists around the lee side. At $\lambda/D = 5$, the total sea surface elevation is dominated by the incident wave, with minimal distortion. The smoother sea surface elevation and less pronounced wave interference around the structure indicate a decreasing influence of the structure on the overall wave field as λ/D increases. Figures 2c and 2d show the scattered potential and kinetic energy for $\lambda/D = 3$, while Figures 3c and 3d present the corresponding fields for $\lambda/D = 5$. As λ/D increases, the scattered energy becomes increasingly concentrated in the backward direction of wave propagation. For $\lambda/D = 3$, most of the scattered wave energy remains confined to in front of the structure, and only limited scattering is observed in the lateral directions

19422466, 2026, 2, Downloaded from https://agupubs.onlinelibrary.wiley.com/doi/10.1029/2025MS005603 by Uppsala University Library, Wiley Online Library on [04/03/2026]. See the Terms and Conditions (https://onlinelibrary.wiley.com/terms-and-conditions) on Wiley Online Library for rules of use; OA articles are governed by the applicable Creative Commons License

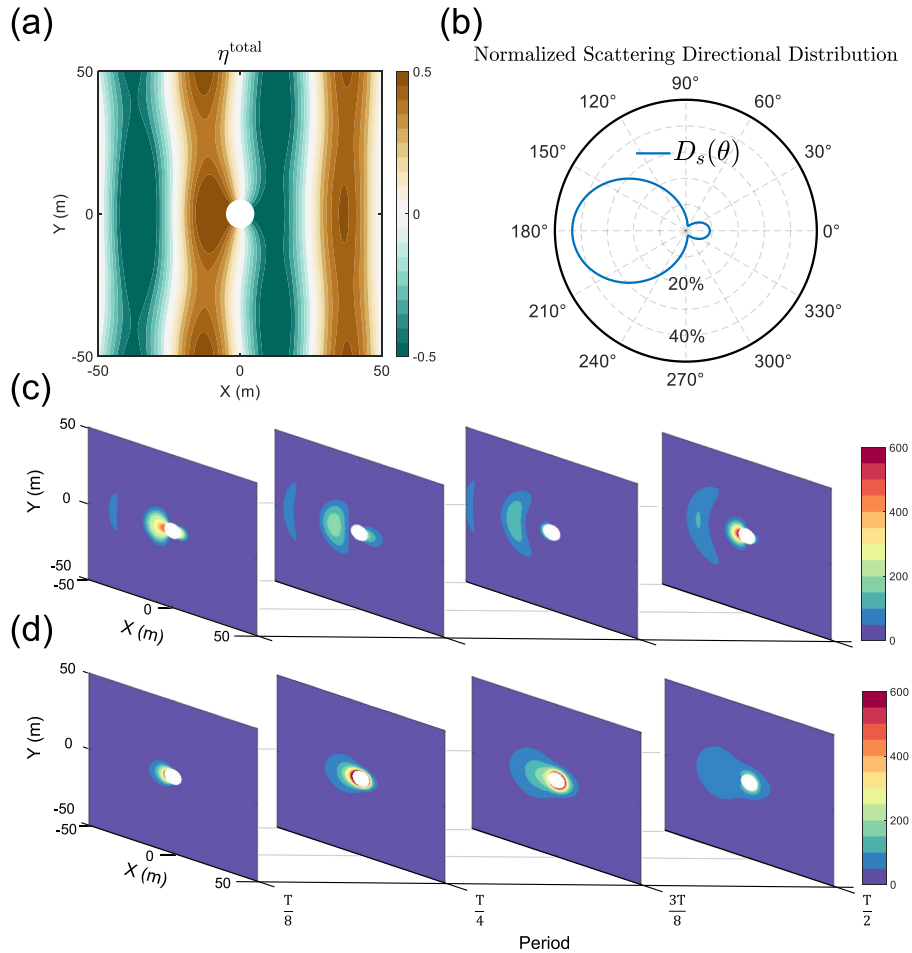

Figure 3. Same as Figure 1, but for $\lambda/D = 5$.

and behind the structure. At $\lambda/D = 5$, the scattered energy is restricted to the region in front of the structure, with negligible energy reaching the lee side. These results reflect the dominance of low-order angular scattering modes in the regime where the wavelength exceeds the structure diameter, with wave energy primarily redistributed along the forward and backward directions, while lateral scattering is significantly reduced. Despite the simplified angular structure, the scattered energy remains distributed over a relatively broad backward sector.

These results demonstrate that wave-structure interactions induce significant angular redistribution of wave energy, with scattering patterns strongly dependent on the ratio of wavelength to structure diameter. Such processes can be directly represented in phase-resolving models, which explicitly resolve the wave field in space and time but are computationally expensive and thus impractical for simulations at wind-farm scales. In contrast, spectral wave models are more efficient and therefore widely used for wind farm and larger scale wave simulations. However, these models cannot explicitly capture the local wave–structure interactions and usually represent offshore structures as purely dissipative obstacles (Alari & Raudsepp, 2012; Hosseini et al., 2025; Ponce de León et al., 2011; Zhao et al., 2024). A natural question therefore arises: can the wave scattering, specifically the directional redistribution of wave energy, be represented within a spectral framework in a energy-conserving manner? To address this, the following section introduces a parameterization scheme designed to capture the essential features of wave scattering while conserving the total wave energy.

19422466, 2026, 2, Downloaded from https://agupubs.onlinelibrary.wiley.com/doi/10.1029/2025MS005603 by Uppsala University Library, Wiley Online Library on [04/03/2026]. See the Terms and Conditions (https://onlinelibrary.wiley.com/terms-and-conditions) on Wiley Online Library for rules of use; OA articles are governed by the applicable Creative Commons License

19422466, 2026, 2, Downloaded from https://agupubs.onlinelibrary.wiley.com/doi/10.1029/2025MS005603 by Uppsala University Library, Wiley Online Library on [04/03/2026]. See the Terms and Conditions (https://onlinelibrary.wiley.com/terms-and-conditions) on Wiley Online Library for rules of use; OA articles are governed by the applicable Creative Commons License

3. Development of Subgrid-Scale Parameterization for Wave-Structure Interaction

Recognizing that wave-structure interactions span a range of physical regimes depending on λ/D, it follows that when the incident wavelength is comparable to the structure diameter, specifically in the range $0 < \lambda/D \leq 5$, wave-structure interactions are dominated by reflection and diffraction processes (Sarpkaya, 2010). In this regime, the presence of the structure substantially modifies the incident wave field, resulting in scattered waves that comprise both reflected and diffracted components. Conversely, when the wavelength is significantly larger than the structure diameter, that is, $\lambda/D > 5$, wave-structure interactions has little influence on propagation characteristics of wave field (Kvittem et al., 2012). The structures do not cause notable scattering, but instead contribute to local energy dissipation through drag and inertia forces acting on waves. Given these distinct interaction regimes, a unified modeling approach must accommodate the underlying physics across different λ/D. To this end, we introduce a parameterization framework that captures the dominant physical mechanisms within each λ/D regimes.

3.1. Wave Scattering Parameterization

In the regime of $1 \leq \lambda/D \leq 5$, the wave diffraction theory (MacCamy & Fuchs, 1954) is used to provide an energy-conserved framework for describing energy redistribution rather than introducing an artificial dissipation term.

The interaction between an incident wave and a cylindrical foundation leads to a redistribution of wave energy. Identifying and quantifying how much energy is scattered away from the incident direction is therefore the first step toward formulating an energy-conserving representation of this process. To this end, a scattering coefficient is introduced. For a wave component with frequency σ, the scattering coefficient $C_s(\sigma)$ is defined as the ratio of scattered wave energy to the incident wave energy

$$C_s(\sigma) = \frac{e^{\text{scat}}(\sigma)}{e^{\text{inc}}(\sigma)} \tag{18}$$

where $e^{\text{scat}}(\sigma)$ and $e^{\text{inc}}(\sigma)$ denote the total scattered and incident wave energies at frequency σ, respectively. By definition, $C_s(\sigma)$ represents the fraction of the total incident energy that is redirected by the structure. Under linear wave theory, potential, and kinetic energy are equal. Therefore, the total energy can be given by $e^{\text{scat}}(\sigma) = 2e_k^{\text{scat}}(\sigma)$ and $e^{\text{inc}}(\sigma) = 2e_k^{\text{inc}}(\sigma)$. The evaluation of these energy terms involves spatial integration over the region surrounding the structure. Physically, the far-field scattered wave field behaves approximately like outgoing waves, with wave energy decreasing with radial distance from the structure. To represent this radial attenuation on a discrete grid, both $e^{\text{scat}}(\sigma)$ and $e^{\text{inc}}(\sigma)$ are computed by integrating over a circular domain of radius R centered on the structure. In this sense, the radial integration limit R actually work as a scaling factor that accommodates the scattering coefficient to the model resolution. In the present implementation, R is set to half of the model grid spacing, so that the integrated energies correspond approximately to the wave energy contained within a single rectangular grid cell. This treatment ensures that the scattering influence remains consistent across different spatial resolutions.

Figure 4a provides a general overview of the behavior of the scattering coefficient $C_s(\sigma)$, which is dependent on the λ/D. The scattering coefficient decreases approximately linearly as λ/D increases, reaching nearly 2% at $\lambda/D = 1$ and dropping to 0.5% for $\lambda/D = 5$. This performance reflects the reduced scattering as the wavelength becomes much larger than the structure diameter, consistent with the applicability of wave diffraction theory. Figure 4b illustrates the sensitivity of $C_s(\sigma)$ to the radial integration limit R normalized by structure diameter D. It can be seen that the scattering coefficient decreases approximately exponentially with increasing R/D, indicating that the scattered energy is spatially localized near the structure. Specifically, increasing the R/D from 5 to 25 leads to a nearly fivefold decrease in $C_s(\sigma)$, from almost 9% to less than 2%.

Once the total fraction of scattered energy has been quantified through the scattering coefficient, the next step is to determine how this scattered energy is redistributed across different propagation directions. The theoretical analysis in Section 2 demonstrated that scattered field generated by the interaction between waves and the cylindrical structure radiates outward in multiple directions, and the scattered wave energy differs at different propagation angle θ. To quantify this directional dependence, we introduce a directional kinetic energy $e_k^{\text{scat}}(\sigma, \theta)$ which measures the portion of scattered energy associated with each direction. This quantity is evaluated by

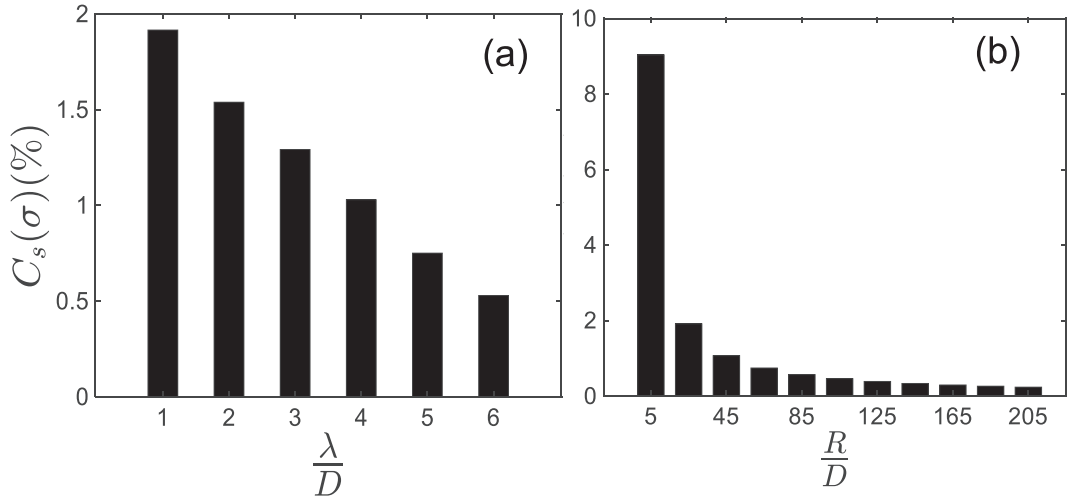

Figure 4. Scattering coefficient characteristics. (a) Dependence of the scattering coefficient on wavelength-to-diameter ratio (λ/D); (b) sensitivity of the scattering coefficient to the ratio pf radial integration limit to turbine diameter (R/D).

integrating the squared velocity components of the scattered field over the water column and radially from the cylinder surface a to an outer radius R:

$$e_k^{\text{scat}}(\sigma,\theta) = \frac{1}{2}\rho \int_{-h}^{0}\int_{a}^{R}\left[\left(u_r^{\text{scat}}\right)^2 + \left(u_\theta^{\text{scat}}\right)^2 + \left(u_z^{\text{scat}}\right)^2\right] r dr dz \tag{19}$$

It represents the scattered kinetic energy density in direction θ. To express how the total scattered energy is partitioned across directions, we normalize $e_k^{\text{scat}}(\sigma,\theta)$ by the total scattered energy $e_k^{\text{scat}}(\sigma)$, This yields the directional redistribution function $D_s(\sigma,\theta)$:

$$D_s(\sigma,\theta) = \frac{e_k^{\text{scat}}(\sigma,\theta)}{e_k^{\text{scat}}(\sigma)} \tag{20}$$

Physically, $D_s(\sigma,\theta)$ represents the relative contribution of scattered energy in each direction. By definition, $D_s(\sigma,\theta)$ satisfies $\int D_s(\sigma,\theta)d\theta = 1$.

As shown in Figures 1b, 2b, and 3b, the normalized directional distribution function $D_s(\sigma,\theta)$ exhibits distinct angular patterns depending on the value of λ/D. For $\lambda/D = 1$, the distribution exhibits a multi-lobed pattern, with energy scattered into the lee side (0°) and front side (180°) of the cylindrical structure, as well as into the lateral sides. Among these, the dominant portion of scattered energy is concentrated on the lee side, reflecting strong diffraction effects and the contribution of multiple angular modes. As λ/D increases to 3, the scattered energy concentrated in a broad lobe near 180°, while lateral and forward scattering are significantly reduced. When $\lambda/D = 5$, only a weak lobe remaining in the forward direction. Compared to the $\lambda/D = 3$ case, the angular spreading becomes even narrower, and the overall scattering pattern exhibits weak anisotropy. This trend reflects the dominance of low-order angular scattering modes as λ/D increases, leading to a more symmetric and nearly isotropic distribution.

With the magnitude of wave scattering quantified by $C_s(\sigma)$ and its angular redistribution described by $D_s(\sigma,\theta)$, the scattering process can now be expressed in terms of its impact on the wave spectrum. In a spectral wave model, as implemented in WAVEWATCH III in this study, this process is introduced through a source term. From an energy-balance perspective, the scattering neither generates nor dissipates energy, rather, it conserves the total wave energy by reallocating it across directions, thereby satisfying the first-principle requirement of energy conservation. Accordingly, the source term is formulated as follows:

19422466, 2026, 2, Downloaded from https://agupubs.onlinelibrary.wiley.com/doi/10.1029/2025MS005603 by Uppsala University Library, Wiley Online Library on [04/03/2026]. See the Terms and Conditions (https://onlinelibrary.wiley.com/terms-and-conditions) on Wiley Online Library for rules of use; OA articles are governed by the applicable Creative Commons License

$$S_{tb}(\sigma,\theta) = \frac{-C_s(\sigma)}{\Delta t}N(\sigma,\theta) + \frac{C_s(\sigma)}{\Delta t}N(\sigma,\theta)\int_0^{2\pi} D_s(\sigma,\theta,\theta')\,\mathrm{d}\theta' \tag{21}$$

where $N(\sigma,\theta)$ denotes the directional wave action density spectrum, defined by $N(\sigma,\theta) = E(\sigma,\theta)/\sigma$, where $E(\sigma,\theta)$ is the wave energy density spectrum. The negative term on the right-hand of Equation 21 represents the removal of energy from the incident direction θ due to scattering, while the positive term represents that this part of energy is redistributed from the incident direction θ' to the direction θ through $D_s(\sigma,\theta)$.

The formulation described above applies to the diffraction-dominated regime, and wave energy is redistributed across multiple directions through scattering. When the wavelength becomes shorter than the structure diameter, that is, $\lambda/D < 1$, The wave-structure interaction therefore transitions toward a reflection-dominated regime, which can be approximated as near-specular reflection (Christensen et al., 2013). Accordingly, the scattering source term is simplified to

$$S_{tb}(\sigma,\theta) = -\frac{C_r D}{\Delta x \Delta t}N(\sigma,\theta) + \frac{C_r D}{\Delta x \Delta t}N(\sigma,\pi-\theta) \tag{22}$$

where Δx is the grid spacing of the model domain. C_r is the reflection coefficient, which controls the proportion of reflected energy. For simplicity, $C_r = 1$ is assumed in this study, representing full reflection of incident wave energy from θ to the opposite direction $\pi - \theta$.

3.2. Drag-Induced Dissipation Parameterization

As the wavelength becomes much larger than the structure diameter ($\lambda/D > 5$), the cylinder is slender relative to the wave scale and scattering becomes negligible. In this regime, the wave-structure interaction is more appropriately explained by the Morison equation (Morison et al., 1950), in which the drag force provides dissipative work (energy loss), whereas the inertia force performs no net work over a wave cycle. This formulation has been widely applied to represent wave attenuation by submerged vegetation and other slender structures (Abdolali et al., 2022; Dalrymple et al., 1984; Mendez & Losada, 2004; Suzuki et al., 2012). Unlike the diffraction regime, where wave energy is redistributed directionally, the dominant effect here is local drag-induced energy dissipation, which is not dependent on wave direction. Accordingly, an additional source term is introduced to account for this process:

$$S_{tb}(\sigma,\theta) = -\frac{1}{16\sqrt{\pi}}ng^2C_dD\left(\frac{k}{\sigma}\right)^3\frac{\sinh^3(kh)+3\sinh(kh)}{3k\cosh^3(kh)}\frac{H_{\mathrm{rms}}(\sigma)^3}{E_{\mathrm{tot}}(\sigma)}N(\sigma,\theta) \tag{23}$$

here C_d is the drag coefficient of the structure, which is set to 1.0 for simplicity. n denotes the number of structures (i.e., wind turbines) per unit area. $E_{\mathrm{tot}}(\sigma)$ is the total wave energy at a given frequency σ, which is obtained by integrating the directional wave energy spectrum $E(\sigma,\theta)$ over all propagation directions as

$$E_{\mathrm{tot}}(\sigma) = \int_0^{2\pi} E(\sigma,\theta)\,\mathrm{d}\theta. \tag{24}$$

The corresponding root-mean-square (rms) wave height $H_{\mathrm{rms}}(\sigma)$ at frequency σ is defined as

$$H_{\mathrm{rms}}(\sigma) = \sqrt{8\,E_{\mathrm{tot}}(\sigma)} \tag{25}$$

The theoretical analysis presented above leads to a parameterization that provides a physics-based representation of wave-structure interaction. The scheme explicitly relates the wave energy redistribution and dissipation to the intrinsic wave properties through the wavelength–diameter ratio λ/D. Implemented as a unified source term in WAVEWATCH III, the parameterization accounts for both scattering and dissipation of wave energy across all spectral components. Moreover, the directional distribution function $D_s(\sigma,\theta)$ can adapt flexibly to the incident wave angle, making the approach applicable to both narrow-banded swells and broad directional wind seas. While the development is grounded in the theoretical analysis of a single cylindrical structure, an important question

19422466, 2026, 2, Downloaded from https://agupubs.onlinelibrary.wiley.com/doi/10.1029/2025MS005603 by Uppsala University Library, Wiley Online Library on [04/03/2026]. See the Terms and Conditions (https://onlinelibrary.wiley.com/terms-and-conditions) on Wiley Online Library for rules of use; OA articles are governed by the applicable Creative Commons License

19422466, 2026, 2, Downloaded from https://agupubs.onlinelibrary.wiley.com/doi/10.1029/2025MS005603 by Uppsala University Library, Wiley Online Library on [04/03/2026]. See the Terms and Conditions (https://onlinelibrary.wiley.com/terms-and-conditions) on Wiley Online Library for rules of use; OA articles are governed by the applicable Creative Commons License

Table 1
Numerical Experiments Summary

Experiment ID	Foundation type	Turbines numbers	Diameter (m)	Grid resolution (m)
Obstruction_G500	Monopile	1	10	500
M1D10_G50	Monopile	1	10	50
M1D10_G100	Monopile	1	10	100
M1D10_G250	Monopile	1	10	250
M1D10_G500	Monopile	1	10	500
M1D20_G500	Monopile	1	20	500
M4D10_G1000	Monopile	4	10	1,000
F1D10_G500	Floating	1	10	500

Note. Experiments vary in turbine foundation type (monopile or floating), number of turbines per model grid cell, foundation diameter, and grid resolution. The experiment names follow a structured naming convention: the prefix "M" or "F" indicates monopile (M) or floating (F) foundation types, followed by a number indicates turbines number in single model grid cell. "D10" or "D20" refers to a diameter (D) of 10 m or 20 m, respectively. The suffix "G500" specifies the grid (G) spacing of 500 m.

remains: how will this parameterization perform when applied to an entire offshore wind farm? In particular, to what extent do factors such as turbine diameter, foundation type, and model resolution influence the overall wave field simulation within the farm? These questions are explored in the following section.

4. Methodology

This section introduces the model setup and experimental design used to evaluate the proposed parameterization. The numerical experiments are conducted using the WAVEWATCH III (Tolman et al., 2002) model under idealized wind farm configurations.

4.1. Model Setup

The third-generation spectral wave model version 6.07 (The WAVEWATCH III® Development Group, 2019) was employed in this study. WAVEWATCH III solves the spectral action density balance equation, which includes the wind input term, the nonlinear wave-wave interaction term, and the dissipation term due to wave breaking. The ST4 source term package (Ardhuin et al., 2010) was selected in this configuration. All simulations were carried out within a 60 km × 40 km rectangular domain with a uniform water depth of 20 m. The spectral space was discretized into 36 directions and 36 frequency bins ranging from 0.04 to 1.16 Hz and the waves was forced by a constant and spatially uniform west wind ($u = 10$ ms^{-1}, $v = 0$). To accelerate the establishment of equilibrium in the wave field, double periodic boundary conditions were applied in both the east-west and north-south directions, in the same way as our previous study (Zhao et al., 2024). In all experiments, the simulations were integrated for 36 hr.

4.2. Experimental Design

A set of idealized numerical experiments was conducted to examine the sensitivity of the proposed wave-structure interaction parameterization (Table 1). These experiments were designed to isolate the effects of parameters, such as wind turbine foundation diameter, turbine type, and turbine array density, on wave energy redistribution and wave attenuation, respectively. A wind farm consisting of a 21 × 21 regular grid of turbines was placed in the model domain as shown in Figure 5. The details of the experimental settings are summarized in Table 1. Each experiment varies in one or more key parameters, including foundation type (monopile or floating), foundation diameter (10 or 20 m), the number of turbines per model grid cell, grid spacing of model domain. A structured naming convention is used to encode this information: the prefix "M" or "F" denotes monopile (M) or floating (F) foundations, followed by a number that indicates the turbine numbers installed a single model grid cell. "D10" and "D20" specify foundation diameters of 10 and 20 m, respectively. While "G500" indicates that the model grid spacing is 500 m. For instance, "M1D10_G500" represents a single monopile foundation with a 10 m diameter, located in a model grid with 500 m spacing, whereas "M4D10_G1000" refers to a four-turbine monopile array

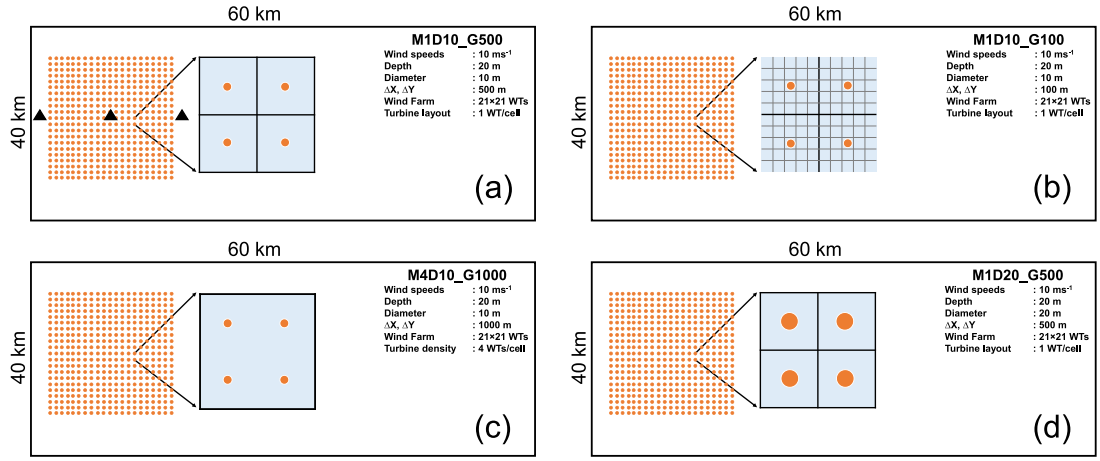

Figure 5. Schematic layout of the model domain and wind farm configuration. (a) Monopile foundation with a diameter of 10 m and a grid spacing of 500 m, (b) monopile foundation with a diameter of 10 m and a grid spacing of 100 m, (c) array of four monopile foundations within a single grid cell, each with a diameter of 10 m and a grid spacing of 1,000 m, (d) monopile foundation with a diameter of 20 m and a grid spacing of 500 m. Wave spectra were extracted at locations upstream, within, and downstream of the wind farm, as indicated by triangles in panel (a).

with 10 m foundation diameters, deployed in a model grid of 1,000 m spacing. Following this naming convention, the experiments are grouped according to the specific parameters tested for sensitivity.

Group 1: Wave scattering. Obstruction_G500, which serves as a reference, provided a baseline to evaluate the effect of wave-structure interactions. It adopted the obstruction approach (Chawla & Tolman, 2008; Tolman, 2003) in WAVEWATCH III, which represents the blocking effect of sub-grid obstacles such as islands. In this method, the obstruction coefficient quantifies the fraction of the cell face blocked by sub-grid obstacles. It is computed based on the ratio between the obstacle size and the model grid spacing, and applied as a multiplicative factor to the wave flux term in the wave action balance equation. In this experiment, a constant obstruction coefficient of 0.02 is used, calculated based on the turbine diameter of 10 m and the model grid spacing of 500 m.

Group 2: Turbine foundation diameter. To assess the influence of turbine foundation diameter, experiment M1D20_G500 used a foundation diameter of 20 m, twice that of M1D10_G500.

Group 3: Multiple turbines. The effect of multiple turbines in a single model grid cell was examined in experiment M4D10_G1000. To maintain the same overall wind farm size as M1D10_G500, four turbines were placed within each mode grid cell with a spacing of 1,000 m in M4D10_G1000. For simplicity, wave scattering was modeled as a sequential process, assuming that each turbine scatters the wave independently, which means no interaction between turbines was considered. Under this assumption, the effective scattering coefficient can be written as

$$C_{s,\mathrm{eff}}(\sigma) = 1 - (1 - C_s(\sigma))^n \tag{26}$$

where n denotes the turbine number per grid cell, which is four in this case. This formulation represents the cumulative increase of the scattering coefficient due to multiple independent scattering along the wave propagation path.

Group 4: Floating turbine foundation. Turbine foundation type effect was evaluated by comparing M1D10_G500 and F1D10_G500, in which the turbines were modeled as floating structures with a shallow submerged depth of 1 m. In this experiment, when computing the scattering coefficient and the directional redistribution function using Equations 8 and 19, the vertical integration was performed from the free surface down to the submerged depth of 1 m, rather than over the full water column as in the monopile cases.

Group 5: Spatial resolution. Grid resolution sensitivity was assessed by comparing cases M1D10_G50, M1D10_G100, M1D10_G250, and M1D10_G500, representing grid spacings of 50, 100, 250, and 500 m, respectively.

19422466, 2026, 2, Downloaded from https://agupubs.onlinelibrary.wiley.com/doi/10.1029/2025MS005603 by Uppsala University Library, Wiley Online Library on [04/03/2026]. See the Terms and Conditions (https://onlinelibrary.wiley.com/terms-and-conditions) on Wiley Online Library for rules of use; OA articles are governed by the applicable Creative Commons License

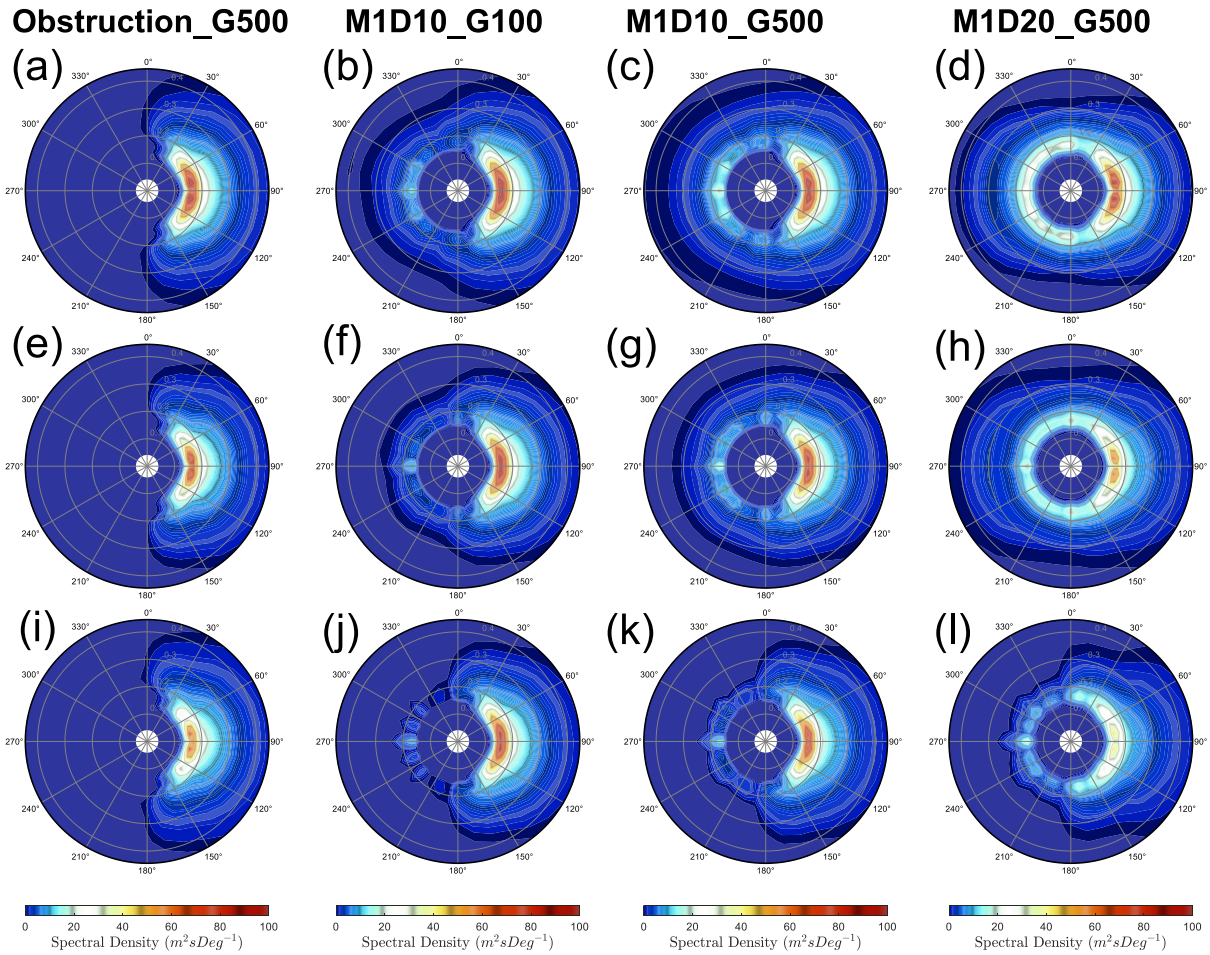

Figure 6. Directional wave spectra at three representative locations: upstream (top row), within (middle row), and downstream (bottom row) of the wind farm. From left to right, the columns correspond to four configurations: (a, e, and i) default setup with grid spacing 500 m, turbine foundations treated as unresolved obstacles, (b, f, and j) monopile foundation, diameter 10 m, grid spacing 100 m, (c, g, and k) monopile foundation, diameter 10 m, grid spacing 500 m, and (d, h, and l) monopile foundation, diameter 20 m, grid spacing 500 m.

5. Results

5.1. Effect of Wave Scattering

To assess the physical validity of the implemented parameterization, directional wave spectra were extracted at three representative locations: upstream, center, and downstream of the wind farm (marked by triangles in Figure 5), with the upstream and downstream points located 5 km from the farm center. These spectra were used to evaluate how wave energy is attenuated and redistributed as waves propagate through the wind farm. Figure 6 presents the wave spectra at these three locations. In the reference experiment (Obstruction_G500), where turbines are treated as sub-grid obstructions without accounting for wave-structure interactions, a substantial reduction in wave energy is observed from the upstream to the downstream of the wind farm (Figures 6a, 6e, and 6i), while retaining a narrow directional distribution centered around the incident direction. This reflects the dissipative effect of the obstruction treatment, where wave energy is partially blocked rather than scattered. In contrast, the experiments that incorporate wave-structure interactions (columns 2–4 in Figure 6) not only reproduce the expected attenuation of wave energy from upstream to downstream, but also exhibit distinct signatures of energy redistribution. Compared to Obstruction_G500, the experiments with the new parameterization exhibit broad angular redistribution of wave energy. Spectral energy appears not only along the incident direction but also across lateral and opposite directions, particularly visible on the left half of the polar plots. These results confirm that the proposed parameterization captures both the attenuation and directional spreading effects of wave-structure interactions.

19422466, 2026, 2, Downloaded from https://agupubs.onlinelibrary.wiley.com/doi/10.1029/2025MS005603 by Uppsala University Library, Wiley Online Library on [04/03/2026]. See the Terms and Conditions (https://onlinelibrary.wiley.com/terms-and-conditions) on Wiley Online Library for rules of use; OA articles are governed by the applicable Creative Commons License

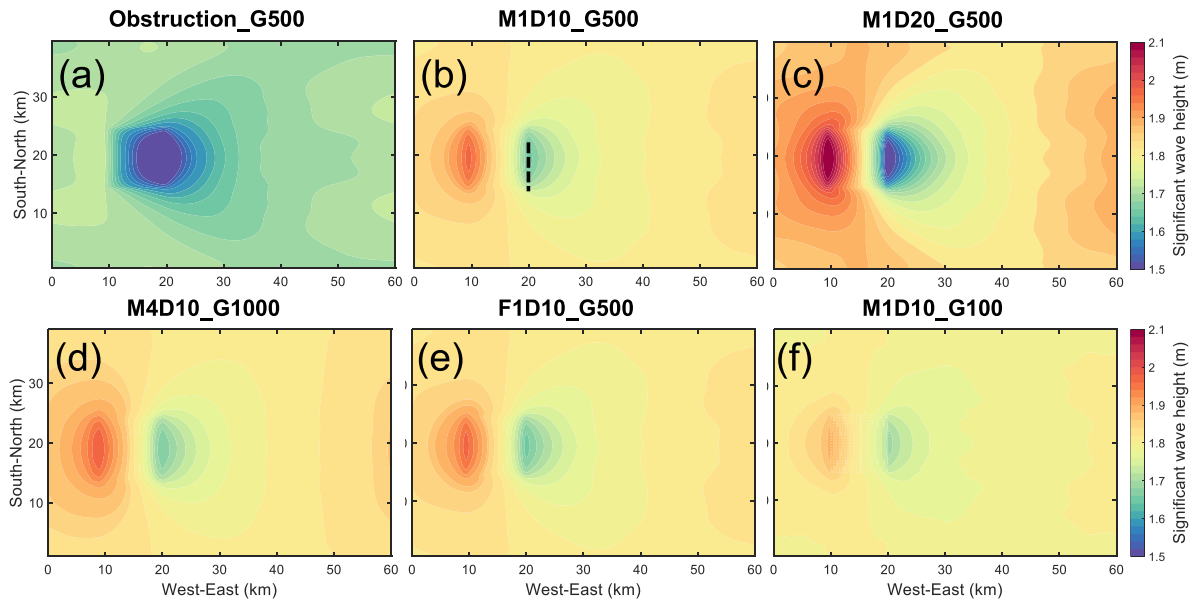

Figure 7. Spatial distribution of significant wave height for six different experiments: (a) default setup, where turbine foundations are treated as unresolved obstacles, grid spacing 500 m, (b) monopile foundation, diameter 10 m, grid spacing 500 m, (c) monopile foundation, diameter 20 m, grid spacing 500 m, (d) four monopile foundations per grid cell, diameter 10 m, grid spacing 1,000 m, (e) floating foundation, diameter 10 m, grid spacing 500 m, and (f) monopile foundation, diameter 10 m, grid spacing 100 m. The downstream significant wave heights of all the experiments were extracted along the transect shown in panel (b).

Figure 7 illustrates the impact of wave-structure interactions on significant wave height. In the reference experiment (Obstruction_G500), the significant wave height is reduced throughout the model domain, with more pronounced attenuation occurring within and in the lee of the wind farm (Figure 7a). In contrast, the experiments with the new parameterization (Figures 7b–7f) reveal a distinct spatial pattern characterized by an upstream enhancement and a more localized reduction in wave height downstream. This pattern reflects the energy-conserving nature of the wave-structure interaction, wherein wave energy is redistributed directionally. The resulting asymmetry in wave height distribution with elevated levels upstream and a shadow zone downstream, is consistent with the theoretical expectations discussed in Sections 2 and 3, confirming that the proposed source term captures the essential wave energy redistribution features of directional scattering.

5.2. Impact of Turbine Foundation Diameter

As discussed in Sections 2 and 3, turbine diameter is a key parameter governing wave attenuation intensity and angular redistribution. By comparing M1D10_G500 and M1D20_G500, it can be seen that increasing the turbine diameter leads to a more pronounced redistribution of wave energy across directions (columns 3 and 4 in Figure 6). Larger-diameter case exhibits a broader angular spread of scattered energy and a more noticeable reduction in spectral intensity along the incident wave direction. This enhanced wave attenuation is also reflected in the spatial distribution of significant wave height (Figures 7b and 7c). Compared to M1D10_G500, the larger-diameter experiment (M1D20_G500) exhibits stronger upstream enhancement and more pronounced downstream attenuation of wave height. This reflects the stronger wave-structure induced by larger structures, which conserves wave energy but scatters more of it into lateral and upstream directions.

To quantify the effect of wave wave-structure on the downstream wave fields, we defined an attenuation ratio

$$A_r = \frac{H_s - H_s^{\mathrm{dw}}}{H_s} \tag{27}$$

where H_s represents the domain-averaged significant wave height, and H_s^{dw} is the averaged value along the downstream transect. In Figure 8, a clear difference in A_r is observed between M1D10_G500 and M1D20_G500.

19422466, 2026, 2, Downloaded from https://agupubs.onlinelibrary.wiley.com/doi/10.1029/2025MS005603 by Uppsala University Library, Wiley Online Library on [04/03/2026]. See the Terms and Conditions (https://onlinelibrary.wiley.com/terms-and-conditions) on Wiley Online Library for rules of use; OA articles are governed by the applicable Creative Commons License

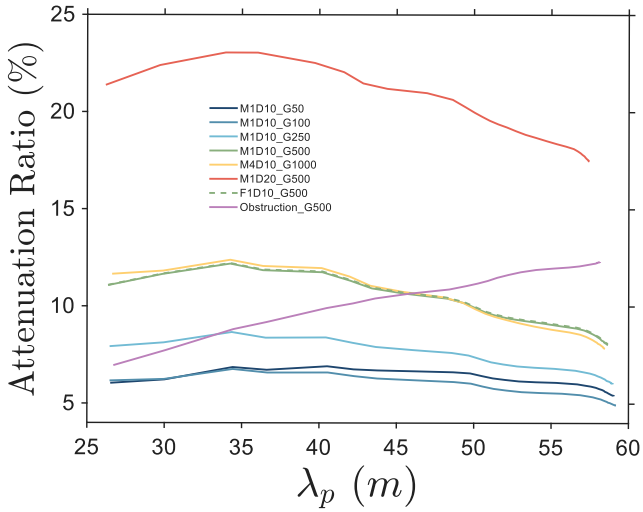

Figure 8. Downstream wave attenuation ratio as a function of peak wavelength for selected experiments. The ratio is computed based on the significant wave height along the transect indicated by the black dashed line in Figure 7b.

The larger foundation diameter results in a greater reduction of significant wave height, with the peak A_r exceeding 22%, compared to approximately 11% in the small-diameter experiment. Additionally, it can be seen that A_r increases with mean wavelength, reaches a peak, and then gradually decreases. This behavior aligns with the parameterization framework described in Section 3, where wave scattering dominates in the regime of $\lambda/D \leq 5$, while drag-induced dissipation becomes dominant beyond this range.

5.3. Effect of Multiple Turbines

Both M1D10_G500 and M4D10_G1000 experiments feature the identical wind farms size and turbine diameter, with M4D10_G1000 representing four turbines within each grid cell, in contrast to one per cell in M1D10_G500. The significant wave height distributions (Figures 7b and 7d) and the downstream reduction A_r (Figure 8) are highly similar between the two cases. This consistency indicates that, due to the spatially localized nature of wave-structure interactions around each turbine, the scattered wave energy does not significantly influence neighboring turbines when the turbine spacing (e.g., 500 m) is sufficiently large. As a result, the cumulative scattering effect of multiple turbines can be largely captured by applying the effective scattering coefficient introduced in Section 3. This suggests the applicability of the proposed parameterization for multiple-turbine representation under sparse turbine spacing. However, as the turbine layout becomes denser, this approximation may no longer hold, and a more finer resolution or more rigorous theoretical treatment is required to account for multiple scattering effects.

5.4. Floating Turbine Foundation

Despite the different turbine foundation types, both Monopile (M1D10_G500) and Floating (F1D10_G500) experiments exhibit nearly identical spatial patterns of wave heights (Figures 7b and 7e) and A_r (Figure 8). These results suggest that, under the current experimental conditions, with a uniform water depth of 20 m and moderate wind forcing (10 ms^{-1}), the wave energy is primarily concentrated near the surface. As a result, the submerged depth change between monopile and floating foundations introduces negligible differences in wave-structure interactions and thus wave fields. However, when the submerged depth of floating structures is further reduced, differences in wave fields begin to emerge. It should be emphasized that the primary objective of this study is not to quantify the sensitivity to foundation type, but to give an idea of the applicability of the proposed parameterization for offshore wind farm configurations.

5.5. Model Resolution

A clear difference in the spatial distribution of significant wave height can be observed between M1D10_G500 (Figure 7b) and M1D10_G100 (Figure 7f), where the only difference lies in the spatial resolution of the wave model. Figure 8 further illustrates the sensitivity of wave attenuation to model resolution by comparing four experiments with identical turbine configurations but varying grid spacings (50, 100, 250, and 500 m). As the resolution increases from 500 to 100 m, A_r decreases systematically (Figure 8). Further refinement from 100 to 50 m yields a peak A_r of about 7%, with minimal difference between the two cases, suggesting that the solution approaches convergence. This resolution-dependent behavior reflects the inherent numerical diffusion resulting from the finite spatial resolution of the model grid.

To verify this hypothesis, two additional simulations were conducted, each using only a single turbine placed within the domain, thereby eliminating the influence of neighboring turbines. As expected, the lower-resolution run exhibited a broader spatial area of wave height reduction but smaller in magnitude, while the high-resolution case showed a much more localized response with a sharper gradient in wave height (not shown). Such behavior also occurs in the traditional approach, where a turbine is represented as an obstacle (obstruction) and the wave energy is dissipated at the corresponding grid cells. In this case, the numerical diffusion tends to spread the energy loss over a wider downstream region than physically expected. Therefore, this phenomenon is not specific to the

19422466, 2026, 2, Downloaded from https://agupubs.onlinelibrary.wiley.com/doi/10.1029/2025MS005603 by Uppsala University Library, Wiley Online Library on [04/03/2026]. See the Terms and Conditions (https://onlinelibrary.wiley.com/terms-and-conditions) on Wiley Online Library for rules of use; OA articles are governed by the applicable Creative Commons License

19422466, 2026, 2, Downloaded from https://agupubs.onlinelibrary.wiley.com/doi/10.1029/2025MS005603 by Uppsala University Library, Wiley Online Library on [04/03/2026]. See the Terms and Conditions (https://onlinelibrary.wiley.com/terms-and-conditions) on Wiley Online Library for rules of use; OA articles are governed by the applicable Creative Commons License

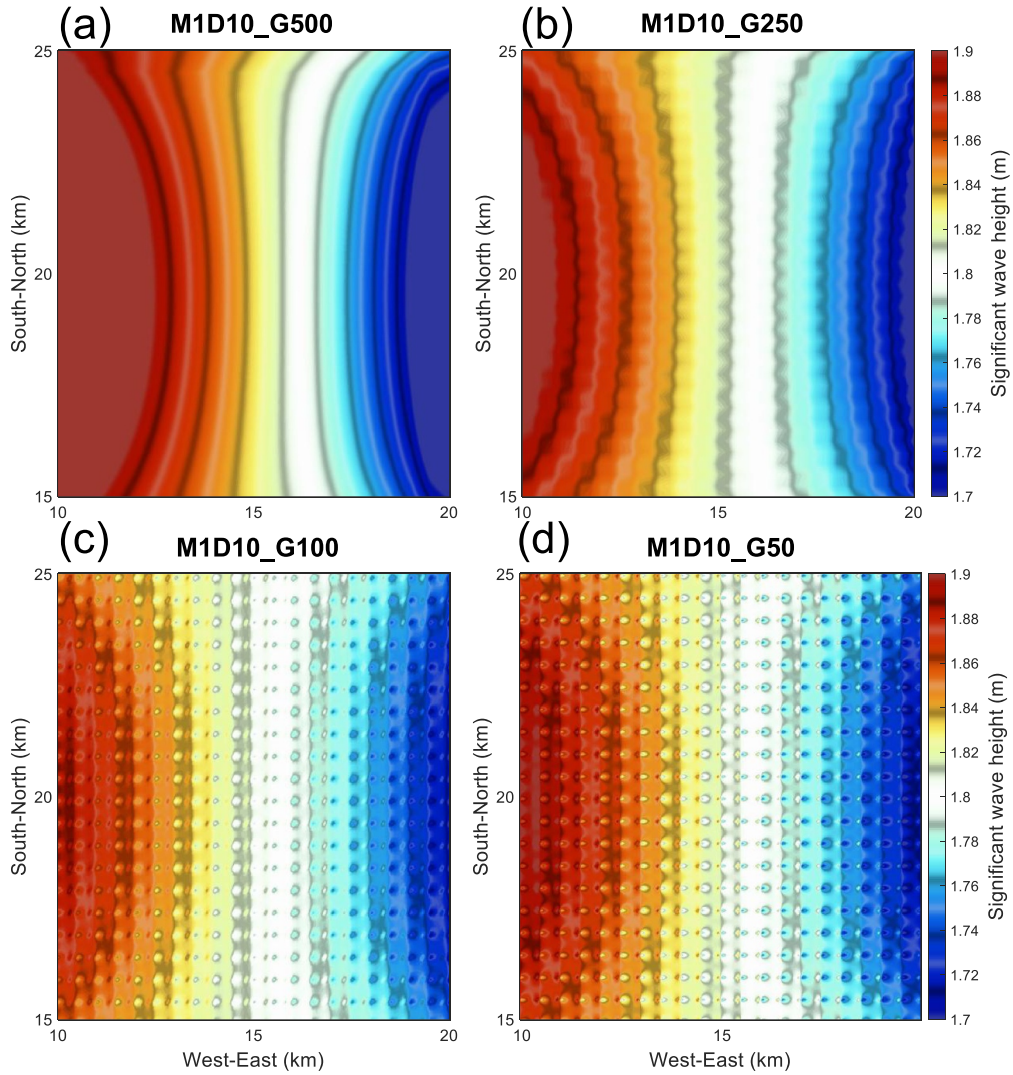

Figure 9. Zoomed-in view of significant wave height fields across the wind farm under varying spatial resolutions: (a) monopile foundation, diameter 10 m, grid spacing 500 m, (b) monopile foundation, diameter 10 m, grid spacing 250 m, (c) monopile foundation, diameter 10 m, grid spacing 100 m, and (d) monopile foundation, diameter 10 m, grid spacing 50 m.

parameterization proposed in this study but rather a typical issue arising from spatial discretization in numerical modeling.

To further demonstrate the impact of model resolution, Figure 9 provides a zoomed-in view of the significant wave height distribution across the wind farm under different model resolutions. At coarse resolutions (Figures 9a and 9b), the model captures only the overall effect of the wind farm, with visible wave height reduction downstream and amplification upstream. As resolution increases (Figures 9c and 9d), the small-scale local variations in wave height emerge around individual turbines. These findings suggest that finer resolution allows the energy redistribution associated with wave-structure interactions to be resolved more explicitly, thereby reducing the overestimation of wave-structure interactions at coarser resolution.

6. Discussion and Conclusion

This study proposed a new parameterization that addresses a long-standing limitation in spectral wave models, where offshore cylindrical structures such as wind turbines and wave converters are often represented as overly simplified energy sinks. The parameterization is physically based and explicitly represents the scale-dependent regimes of wave–structure interaction governed by the wave–structure scale ratio (λ/D). In the scattering-

19422466, 2026, 2, Downloaded from https://agupubs.onlinelibrary.wiley.com/doi/10.1029/2025MS005603 by Uppsala University Library, Wiley Online Library on [04/03/2026]. See the Terms and Conditions (https://onlinelibrary.wiley.com/terms-and-conditions) on Wiley Online Library for rules of use; OA articles are governed by the applicable Creative Commons License

dominated regime (λ/D $\leq$ 5), where the wavelength is comparable to the structural scale, the formulation is based on wave diffraction theory and implemented as an energy-conserving source term. It incorporates a scattering coefficient and a normalized directional redistribution function to represent directional energy redistribution. When λ/D falls below 1, the interaction is approximated as near-specular reflection, with energy redirected opposite to the incident direction. When wavelength becomes much larger than the structure scale (λ/D > 5), scattering becomes negligible and energy loss due to drag forcing becomes the dominant process, which is represented by a dissipative source term. The above two regimes were formulated within a unified source term and implemented in WAVEWATCH III, offering a more realistic basis for simulating wave conditions in offshore renewable energy applications.

A series of idealized numerical experiments was then conducted to evaluate the sensitivity of wave response to turbine diameter, foundation type, array density, and model resolution. The simulations demonstrate that the proposed parameterization reproduces key physical signatures of wave-structure interactions. In contrast, commonly used energy-sink approaches, such as representing turbines as obstructions, introduce artificial dissipation, leading to an overall reduction of wave energy throughout the model domain, particularly in the lee of the wind farm. With the new parameterization, wave spectra extracted at upstream, within, and downstream locations clearly show broader directional spreading and redistribution of wave energy, particularly in lateral and opposite directions. These features are consistent with the expectations from theoretical analysis and support the physical realism of the implemented source term. This directional redistribution of energy manifests as a distinct spatial pattern in significant wave height, with amplification upstream of the farm and attenuation downstream.

Simulations highlight that adequate model resolution is important for ensuring the physical realism of simulated wave–structure interaction. As grid spacing decreases, the downstream attenuation of wave height gradually converges, while coarser resolutions exhibit enhanced upstream amplification and downstream attenuation in wave height due to numerical diffusion inherent to spatial discretization. These results indicate that the proposed parameterization is more suitable for wind farm scale and regional applications, where explicit representation of wave–structure interactions is essential for accurately modeling the wave field. From a practical perspective, the results suggest that the grid spacing should be comparable to the distance over which the scattered wave energy decays to negligible levels. For large-scale applications, where an entire wind farm may fall within a single grid cell, the question becomes a trade-off between physical fidelity and necessity, depending on the intended purpose of the study.

The present experiments were conducted under a uniform wind speed of 10 ms^{-1}. It can be reasonably inferred from Figure 8 that increasing wind speed will shift the spectral peak toward lower frequencies, leading to longer wavelengths. This will result in increased λ/D, under which scattering becomes negligible and drag-induced dissipation emerges as the dominant mechanism. Consequently, downstream wave height attenuation is expected to be less pronounced under strong wind conditions. Nevertheless, the proposed parameterization is not restricted to the idealized conditions considered in this study. Because it is formulated in spectral form and depends only on wave properties and structure scale, it can accommodate complex directional sea states, including both narrow-banded swells and broad, multidirectional wind seas.

The lack of direct observational evidence for wave-structure interactions in operational offshore wind farms limits our ability to validate the proposed parameterization. Wave-structure interactions by structures can be described using wave diffraction theory, which has been validated in laboratory wave experiments (Han et al., 2024; Qin et al., 2023) and widely applied in fields such as optics, acoustics, and electromagnetics (Chaplain et al., 2025; Szulzycki et al., 2016; Tabatadze et al., 2023). However, wave-structure interactions under real offshore wind farms have not yet been confirmed through observation. This gap is likely due to the high cost and technical challenges of offshore measurements, particularly the difficulty of separating scattering-induced energy redistribution from natural directional spreading in wave spectra. As a result, validating the parameterization developed in this study remains a significant challenge. Addressing this issue will require coordinated efforts across the research community, combining field observations, remote sensing, laboratory experiments, theoretical analysis, and numerical modeling.

The assumption of independent scattering, where each turbine affects waves individually without interacting with others, works well under sparse turbine spacing, but its validity becomes questionable in more compact layouts. In the coarser resolution experiment with multiple turbines per grid, the effective scattering coefficient approach

19422466, 2026, 2, Downloaded from https://agupubs.onlinelibrary.wiley.com/doi/10.1029/2025MS005603 by Uppsala University Library, Wiley Online Library on [04/03/2026]. See the Terms and Conditions (https://onlinelibrary.wiley.com/terms-and-conditions) on Wiley Online Library for rules of use; OA articles are governed by the applicable Creative Commons License

produced results comparable to higher-resolution simulations with a single turbine per grid, supporting its use in low-density layouts. However, this assumption may break down in high-density layouts, such as wave energy converter arrays, where the spacing between converters is relatively small and scattered waves from one device can interact with others (Babarit, 2013). These array interaction effects may lead to more complex spatial redistribution patterns. In addition to increasing model resolution, existing theoretical frameworks, such as multiple scattering theory for cylinder arrays (Dalrymple Robert et al., 2015; Linton & Evans, 1990; Porter et al., 2022), provide a basis for addressing such effects. Incorporating these approaches can expand the applicability of the parameterization to scenarios with high-density arrays.

Another open question is the relative contribution of wave-structure interactions and turbine wake effects to wave energy attenuation within and downstream of offshore wind farms. Two distinct mechanisms are involved: direct wave-structure interactions and indirect attenuation due to wind speed deficits in atmospheric wakes, which suppress wave growth. While our results highlight that wave-structure interactions lead to localized energy redistribution and significant wave height reduction in the lee side of the wind farm, previous studies (Fischereit et al., 2022; Larsén et al., 2024) have shown that wind speed deficits in turbine wakes can also reduce wave height over longer distances. A key open question is the relative importance and spatial scales of these two mechanisms, whether wave-structure interactions dominate near-field attenuation and wake-induced forcing governs far-field effects, or vice versa. Quantifying their contributions requires further investigation, potentially through high-resolution coupled air-wave modeling frameworks that explicitly resolve wind farm-wave-atmosphere feedback.

Conflict of Interest

The authors declare no conflicts of interest relevant to this study.

Data Availability Statement

The WAVEWATCH III model is publicly available at https://github.com/NOAA-EMC/WW3. The source code for the parameterization proposed in this study is available on Zenodo at https://doi.org/10.5281/zenodo.18174026 (Zhao, 2026b). An implementation of the parameterization, along with documentation and an example test case, is available in the GitHub repository (https://github.com/Biao-Zhao/WaveF). The scripts and programs used to process the model output and generate the figures in this study are publicly available on Zenodo at https://doi.org/10.5281/zenodo.18237493 (Zhao, 2026a).

Acknowledgments
Biao Zhao gratefully acknowledges support from the Carl Trygger Foundation through Grant CTS22:2049, which funded his research stay in Sweden. The computations were performed using resources provided by the National Academic Infrastructure for Supercomputing in Sweden (NAISS), partially funded by the Swedish Research Council through grant agreement no. 2022-06725. We also acknowledge support from the StandUp for Wind research program. We thank the editor and the anonymous reviewers for their careful and constructive reviews, which substantially improved the clarity and quality of this manuscript.

References

Abdolali, A., Hesser, T. J., Anderson Bryant, M., Roland, A., Khalid, A., Smith, J., et al. (2022). Wave attenuation by vegetation: Model implementation and validation study. *Frontiers in Built Environment*, *8*, 891612. https://doi.org/10.3389/fbuil.2022.891612

Alari, V., & Raudsepp, U. (2012). Simulation of wave damping near coast due to offshore wind farms. *Journal of Coastal Research*, *28*(1), 143–148. https://doi.org/10.2112/JCOASTRES-D-10-00054.1

Ardhuin, F., Rogers, E., Babanin, A. V., Filipot, J. F., Magne, R., Roland, A., et al. (2010). Semiempirical dissipation source functions for ocean waves. Part I: Definition, calibration, and validation. *Journal of Physical Oceanography*, *40*(9), 1917–1941. https://doi.org/10.1175/2010JPO4324.1

Astariz, S., Perez-Collazo, C., Abanades, J., & Iglesias, G. (2015). Co-located wind-wave farm synergies (operation & maintenance): A case study. *Energy Conversion and Management*, *91*, 63–75. https://doi.org/10.1016/j.enconman.2014.11.060

Babarit, A. (2013). On the park effect in arrays of oscillating wave energy converters. *Renewable Energy*, *58*, 68–78. https://doi.org/10.1016/j.renene.2013.03.008

Cavaleri, L., Fox-Kemper, B., & Hemer, M. (2012). Wind waves in the coupled climate system. *Bulletin of the American Meteorological Society*, *93*(11), 1651–1661. https://doi.org/10.1175/BAMS-D-11-00170.1

Chaplain, G. J., Hawkins, S. C., Peter, M. A., Bennetts, L. G., & Starkey, T. A. (2025). Acoustic lattice resonances and generalised Rayleigh–Bloch waves. *Communications Physics*, *8*(1), 37. https://doi.org/10.1038/s42005-025-01950-4

Chawla, A., & Tolman, H. L. (2008). Obstruction grids for spectral wave models. *Ocean Modelling*, *22*(1), 12–25. https://doi.org/10.1016/j.ocemod.2008.01.003

Christensen, E. D., Johnson, M., Sørensen, O. R., Hasager, C. B., Badger, M., & Larsen, S. E. (2013). Transmission of wave energy through an offshore wind turbine farm. *Coastal Engineering*, *82*, 25–46. https://doi.org/10.1016/j.coastaleng.2013.08.004

Dalrymple, R. A., Kirby, J., & Hwang, P. (1984). Wave diffraction due to areas of energy dissipation. *Journal of Waterway Port Coastal and Ocean Engineering-ASCE*, *110*(1), 110–179. https://doi.org/10.1061/(ASCE)0733-950X(1984)110:1(67)

Dalrymple, R. A., Seo Seung, N., & Martin Paul, A. (2015). Water wave scattering by rows of circular cylinders. *Coastal Engineering 1988*, 2216–2228. https://doi.org/10.1061/9780872626874.165

David, D. R., Rijnsdorp, D. P., Hansen, J. E., Lowe, R. J., & Buckley, M. L. (2022). Predicting coastal impacts by wave farms: A comparison of wave-averaged and wave-resolving models. *Renewable Energy*, *183*, 764–780. https://doi.org/10.1016/j.renene.2021.11.048

Dean, R. G., & Dalrymple, R. A. (1991). Water wave mechanics for engineers and scientists. *World Scientific*. https://doi.org/10.1142/1232

Fischereit, J., Larsén, X. G., & Hahmann, A. N. (2022). Climatic impacts of wind-wave-wake interactions in offshore wind farms (Vol. *10*). https://doi.org/10.3389/fenrg.2022.881459

Han, S.-Y., Bouscasse, B., Leroy, V., & Le Touzé, D. (2024). Linear diffraction and radiation theory of water waves by a truncated vertical circular cylinder with heave plate in deep and shallow drafts. *International Journal of Naval Architecture and Ocean Engineering*, *16*, 100580. https://doi.org/10.1016/j.ijnaoe.2023.100580

Hosseini, S. T., Pein, J., Staneva, J., Zhang, Y. J., & Stanev, E. (2025). Impact of offshore wind farm monopiles on hydrodynamics interacting with wind-driven waves. *Ocean Modelling*, *195*, 102521. https://doi.org/10.1016/j.ocemod.2025.102521

Janssen, P. (2004). *The interaction of ocean waves and wind*. Cambridge University Press.

Kvittem, M. I., Bachynski, E. E., & Moan, T. (2012). Effects of hydrodynamic modelling in fully coupled simulations of a semi-submersible wind turbine. *Energy Procedia*, *24*, 351–362. https://doi.org/10.1016/j.egypro.2012.06.118

Larsén, X. G., Fischerelt, J., Hamzeloo, S., Bärfuss, K., & Lampert, A. (2024). Investigation of wind farm impacts on surface waves using coupled numerical simulations. *Renewable Energy*, *237*, 121671. https://doi.org/10.1016/j.renene.2024.121671

Linton, C. M., & Evans, D. V. (1990). The interaction of waves with arrays of vertical circular cylinders. *Journal of Fluid Mechanics*, *215*, 549–569. https://doi.org/10.1017/S0022112090002750

MacCamy, R. C., & Fuchs, R. A. (1954). *Wave forces on piles: A diffraction theory (technical report)*. US Beach Erosion Board.

Mendez, F. J., & Losada, I. J. (2004). An empirical model to estimate the propagation of random breaking and nonbreaking waves over vegetation fields. *Coastal Engineering*, *51*(2), 103–118. https://doi.org/10.1016/j.coastaleng.2003.11.003

Morison, J. R., Johnson, J. W., & Schaaf, S. A. (1950). The force exerted by surface waves on piles. *Journal of Petroleum Technology*, *2*(5), 149–154. https://doi.org/10.2118/950149-G

Neill, S., Robins, P., & Fairley, I. (2017). The impact of marine renewable energy extraction on sediment dynamics. In *Marine renewable energy* (pp. 279–304). Springer International Publishing. https://doi.org/10.1007/978-3-319-53536-4_12

Ponce de León, S., Bettencourt, J. H., & Kjerstad, N. (2011). Simulation of irregular waves in an offshore wind farm with a spectral wave model. *Continental Shelf Research*, *31*(15), 1541–1557. https://doi.org/10.1016/j.csr.2011.07.003

Porchetta, S., Muñoz-Esparza, D., Munters, W., van Beeck, J., & van Lipzig, N. (2021). Impact of ocean waves on offshore wind farm power production. *Renewable Energy*, *180*, 1179–1193. https://doi.org/10.1016/j.renene.2021.08.111

Porter, R., Zheng, S., & Greaves, D. (2021). Extending limits for wave power absorption by axisymmetric devices. *Journal of Fluid Mechanics*, *924*, A39. https://doi.org/10.1017/jfm.2021.645

Porter, R., Zheng, S., & Liang, H. (2022). Scattering of surface waves by a vertical truncated structured cylinder. *Proceedings of the Royal Society A: Mathematical, Physical and Engineering Sciences*, *478*(2258), 20210824. https://doi.org/10.1098/rspa.2021.0824

Qin, Z., Qian, C., Shen, L., Wang, X., Kaminer, I., Chen, H., & Wang, H. (2023). Superscattering of water waves. *National Science Review*, *10*(7), nwac255. https://doi.org/10.1093/nsr/nwac255

Renzi, E. (2023). Extreme wave formation past a submerged circular sill: The role of linear spatial focusing and resonant trapping. *Physics of Fluids*, *35*(8), 086601. https://doi.org/10.1063/5.0160083

Renzi, E., & Dias, F. (2012). Resonant behaviour of an oscillating wave energy converter in a channel. *Journal of Fluid Mechanics*, *701*, 482–510. https://doi.org/10.1017/jfm.2012.194

Sarpkaya, T. S. (2010). *Wave forces on offshore structures*. Cambridge University Press. https://doi.org/10.1017/CBO9781139195898

Suzuki, T., Zijlema, M., Burger, B., Meijer, M. C., & Narayan, S. (2012). Wave dissipation by vegetation with layer schematization in swan. *Coastal Engineering*, *59*(1), 64–71. https://doi.org/10.1016/j.coastaleng.2011.07.006

Szulzycki, K., Savaryn, V., & Grulkowski, I. (2016). Generation of dynamic bessel beams and dynamic bottle beams using acousto-optic effect. *Optics Express*, *24*(21), 23977–23991. https://doi.org/10.1364/OE.24.023977

Tabatadze, V., Alperen, O. F., & Karaguha, K. (2023). Electromagnetic scattering of h-polarised cylindrical wave by a double-sided impedance circular strip. *IET Microwaves, Antennas & Propagation*, *17*(15), 1093–1105. https://doi.org/10.1049/mia2.12425

The WAVEWATCH III® Development Group. (2019). *User manual and system documentation of WAVEWATCH III® version 6.07 (Technical Note No. 333)*. NOAA/NWS/NCEP/MMAB.

Tolman, H. L. (2003). Treatment of unresolved islands and ice in wind wave models. *Ocean Modelling*, *5*(3), 219–231. https://doi.org/10.1016/S1463-5003(02)00040-9

Tolman, H. L., Balasubramaniyan, B., Burroughs, L. D., Chalikov, D. V., Chao, Y. Y., Chen, H. S., & Gerald, V. M. (2002). Development and implementation of wind-generated ocean surface wave modelsat ncep. *Weather and Forecasting*, *17*(2), 311–333. https://doi.org/10.1175/1520-0434(2002)017⟨0311:DAIOWG⟩2.0.CO;2

van Berkel, J., Burchard, H., Christensen, A., Mortensen, L. O., Petersen, O. S., & Thomsen, F. (2020). The effects of offshore wind farms on hydrodynamics and implications for fishes. *Oceanography*, *33*(4), 108–117. https://doi.org/10.5670/oceanog.2020.410

Venugopal, V., Nemalidinne, R., & Vögler, A. (2017). Numerical modelling of wave energy resources and assessment of wave energy extraction by large scale wave farms. *Ocean & Coastal Management*, *147*, 37–48. https://doi.org/10.1016/j.ocecoaman.2017.03.012

Wu, L., Sahlée, E., Nilsson, E., & Rutgersson, A. (2024). A review of surface swell waves and their role in air-sea interactions. *Ocean Modelling*, *190*, 102397. https://doi.org/10.1016/j.ocemod.2024.102397

Zhao, B. (2026a). Data processing code for: A subgrid-scale parameterization of wave-structure interactions for spectral wave models: Idealized simulations in offshore wind farm conditions v1.0 [Software]. *Zenodo*. https://doi.org/10.5281/zenodo.18237493

Zhao, B. (2026b). A subgrid-scale parameterization of wave-structure interactions for spectral wave models v1.0 [Software]. *Zenodo*. https://doi.org/10.5281/zenodo.18174026

Zhao, B., Sahlée, E., Du, J., & Wu, L. (2024). Wind stress modification by offshore wind turbines: A numerical study of wave blocking impacts. *Ocean Engineering*, *313*, 119651. https://doi.org/10.1016/j.oceaneng.2024.119651

19422466, 2026, 2, Downloaded from https://agupubs.onlinelibrary.wiley.com/doi/10.1029/2025MS005603 by Uppsala University Library, Wiley Online Library on [04/03/2026]. See the Terms and Conditions (https://onlinelibrary.wiley.com/terms-and-conditions) on Wiley Online Library for rules of use; OA articles are governed by the applicable Creative Commons License